

# Alignments of Galaxy Group Shapes with Large Scale Structure

Dante J. Paz<sup>1\*</sup>, Mario A. Sgró<sup>1</sup>, Manuel Merchán<sup>1</sup>, Nelson Padilla<sup>2</sup>

<sup>1</sup> *Instituto de Astronomía Teórica y Experimental (UNC-CONICET), Observatorio Astronómico de Córdoba, Laprida 854, Córdoba, X500BGR, Argentina*

<sup>2</sup> *Departamento de Astronomía y Astrofísica, Universidad Católica de Chile, Vicuña Mackenna 4860, Santiago, Chile.*

Accepted — . Received —

## ABSTRACT

In this paper we analyse the alignment of galaxy groups with the surrounding large scale structure traced by spectroscopic galaxies from the Sloan Digital Sky Survey Data Release 7. We characterise these alignments by means of an extension of the classical two-point cross-correlation function, developed by Paz et al. (2008). We find a strong alignment signal between the projected major axis of group shapes and the surrounding galaxy distribution up to scales of 30 Mpc  $h^{-1}$ . This observed anisotropy signal becomes larger as the galaxy group mass increases, in excellent agreement with the corresponding predicted alignment obtained from mock catalogues and  $\Lambda$ CDM cosmological simulations. These measurements provide new direct evidence of the adequacy of the gravitational instability picture to describe the large-scale structure formation of our Universe.

**Key words:** galaxies: groups: general, dark matter, large-scale structure of universe.

## 1 INTRODUCTION

The majority of studies of clusters of galaxies have assumed they are the visible component of a gravitationally bound system dominated by a dark matter halo. It is well known that these objects exhibit mildly aspherical shapes, with a slight preference toward prolate forms. Moreover, it has been shown that their orientations are related to the surrounding structures such as filaments and large-scale walls (Colberg et al. 2005; Kasun & Evrard 2005; Basilakos et al. 2006; Allgood et al. 2006; Altay et al. 2006; Aragón-Calvo et al. 2007; Brunino et al. 2007; Bett et al. 2007; Zhang et al. 2009). Results from numerical simulations by van Haarlem & van de Weygaert (1993, see also Splinter et al. 1997) have shown that the origin for such alignments comes from the rearrangement of dark matter halo axes in the direction from where matter was predominantly accreted (i.e. last major merger event). Using numerical simulations, several authors have found that dark matter halos tend to be more prolate and aspherical when larger halo masses are considered (Kasun & Evrard 2005; Paz et al. 2006, and references therein). This trend is consistent with the picture described above, and could be easily understood as the result of the accretion process driven

by mergers. After a merger occurs, dynamical relaxation will tend to drive a halo closer to isotropy. Therefore, it is expected that dynamically younger systems will be more strongly ellipsoidal than dynamically older ones. Given that the dynamical age of a system depends on how much time has elapsed from the moment of the last halo merger, it is expected that high-mass halos will tend to be more elongated than lower mass halos.<sup>1</sup> Paz et al. (2006) also found that this predicted trend is consistent with observational results obtained from samples of galaxy groups. More recently, Robotham et al. (2008) confirms this agreement between galaxy group shapes and simulated dark matter halos. Moreover Ragone-Figueroa et al. (2010) found that less concentrated groups, corresponding to later formation times, show lower velocity dispersions and higher elongations than groups of the same mass with higher values of concentration, which correspond to earlier formation times. Therefore, in a statistical sense, the shapes of galaxy groups and their alignments could encode information about the formation of large-scale structure (LSS).

Binggeli (1982) was the first to investigate alignments of pairs of clusters close to each other. Taking 44 Abell groups, Binggeli found that galaxies separated by up to

<sup>1</sup> Small halos may start their development later than higher mass systems (Lagos et al. 2009), but the former will still be subject to a lower number of major mergers (De Lucia et al. 2006).

\* E-mail: dpaz@oac.uncor.edu

30 Mpc show a strong alignment, while the orientation of a given cluster is related to the spatial distribution of neighbour systems. With some exceptions, for example Struble & Peebles (1985) or Rhee & Katgert (1987), most papers in the literature confirm this result (de Theije et al. 1995; West 1989a; Rhee et al. 1992; Onuora & Thomas 2000; West et al. 1995). Other authors (Rhee & Katgert 1987; West 1989b,a; Richstone et al. 1992; Plionis 1994) also reported both, alignment between neighbour clusters, as well as alignments with other groups embedded in the same supercluster. For instance, using 48 superclusters West (1989a) found a tendency for groups to be aligned on scales as large as  $60 \text{ Mpc } h^{-1}$ . More recently Godłowski & Flin (2010) analysed the orientation of galaxy groups in the Local Supercluster, finding strong correlations with the distribution of neighbouring groups up to scales of about 20 Mpc. Using the fourth Release of the Sloan Digital Sky Survey (SDSS, York & et al. 2000), Wang et al. (2009) report several types of alignment signals between pairs of neighbouring galaxy groups and between groups and their surrounding galaxies.

On the other hand, there is an extensive amount of work studying the presence of alignments between halo shapes and the large scale structure using numerical simulations (Aragón-Calvo et al. 2007; Hahn et al. 2007; Brunino et al. 2007; Cuesta et al. 2008; Patiri et al. 2006; Basilakos et al. 2006). Most of these studies perform statistics on the inclinations of halo axes with respect to directions defined by the surrounding structure. This structure is characterised by the particle distribution through various topological signatures such as filaments, walls or voids. While these studies agree on the presence of alignments within the  $\Lambda$ CDM context, the magnitude of the alignment effect depends strongly on the definition of the surrounding structure.

In this paper we report measurements of alignments between galaxy group shapes and the surrounding galaxy distribution in both, real galaxy groups obtained from the seventh data release of the Sloan Digital Sky Survey (SDSS-DR7, Abazajian & et al. 2009) and from a numerical simulation. This is carried out following a methodology similar to those developed in Paz et al. (2008), where the two-point correlation function was used to quantify the alignment between galaxy angular momenta and the large scale structure in both, numerical simulations and real data. In the present work we perform similar measurements, by using the “anisotropic” cross-correlation functions between galaxy groups and individual galaxies, in the directions parallel and perpendicular to the major axis of the group shape. Due to we are only interested in the alignment between galaxy groups and the surrounding large scale structure, we focus our analysis on observed anisotropies over the two halo term of the two-point cross-correlation function. The advantage of this approach is the independence on any particular characterisation of the surrounding structure. Furthermore, this modified two-point cross-correlation function allows a robust comparison between numerical simulations and observational data. A similar procedure to the one presented by Paz et al. (2008), was also applied by Faltenbacher et al. (2009).

## 2 $\Lambda$ CDM PREDICTIONS FOR HALO SHAPE-LSS ALIGNMENTS

In this section we use a numerical simulation to study the anisotropy of the halo-particle cross-correlation function. The anisotropy signal around halos is characterised by taking into account the relative orientation of a particle position with respect to the shape of the central halo. In order to mimic the observational effects on the anisotropy signal, we also analyse the distribution of galaxies around galaxy groups on a SDSS mock catalogue by means of the projected group-galaxy cross-correlation function.

### 2.1 Numerical simulation

Throughout this work we use a collisionless numerical simulation covering a periodic volume of  $500^3 (h^{-1}\text{Mpc})^3$ . The initial conditions at redshift  $\sim 50$  were calculated assuming a spatially flat low-density Universe, with a matter and vacuum density parameters  $\Omega_m = 1 - \Omega_\Lambda = 0.258$ , Hubble constant  $H_0 = 71.9 \text{ km s}^{-1} \text{ Mpc}^{-1}$ , and normalisation parameter  $\sigma_8 = 0.796$ . The resulting particle resolution is  $m_p = 6.67 \times 10^{10} h^{-1} M_\odot$ . The run was performed using the second version of the GADGET code developed by Springel (2005), with a gravitational softening of  $0.03h^{-1}\text{Mpc}$  chosen by following Power et al. (2003).

The identification of particle clumps was carried out by means of a standard friends-of-friends algorithm with a percolation length given by  $l = 0.17 \bar{\nu}^{-1/3}$ , where  $\bar{\nu}$  is the mean number density of DM particles. In order to obtain reliable measurements of halo shapes (as is described below), we only consider halos with at least 30 particle members. Consequently the resulting halo sample has a minimum mass threshold of  $\sim 2 \times 10^{12} h^{-1} M_\odot$ . Nevertheless we are mainly interested in the observed galaxy group mass range, that is between  $10^{13}$  to  $10^{15} h^{-1} M_\odot$  (see figure 3). Therefore our results can be associated with masses ranging from small galaxy groups to galaxy clusters.

Several authors (Warren et al. 1992; Thomas et al. 1998; Hopkins et al. 2005; Allgood et al. 2006; Kasun & Evrard 2005; Lau et al. 2010; Paz et al. 2006, and references therein) have analysed the properties of halo shapes using the best-fitting ellipsoid to the spatial distribution of halo members. Following this standard method, we calculate the shape tensor for each dark-matter halo using the positions of each of its particle members. This can be written as a symmetric matrix,

$$I_{ij} = (1/N_h) \sum_{\alpha=1}^{N_h} X_{\alpha i} X_{\alpha j}, \quad (1)$$

where  $X_{\alpha i}$  is the  $i^{\text{th}}$  component of the displacement vector of a particle  $\alpha$  relative to the centre of mass, and  $N_h$  is the number of particles in the halo. The matrix eigenvalues correspond to the square of the axis ( $a, b, c$  where  $a > b > c$ ) of the characteristic ellipsoid that best describes the spatial distribution of the halo members. Our alignment analysis is based on the eigenvector directions ( $\hat{a}, \hat{b}$  and  $\hat{c}$ ). A fixed  $b/a = 1$  with an arbitrary value of  $c/b$ , corresponds to perfect oblate ellipsoids. On the other hand, systems with fixed  $c/b = 1$  are perfect prolate ellipsoids. A system with  $b/a < c/b$  is associated to a general triaxial ellipsoid with

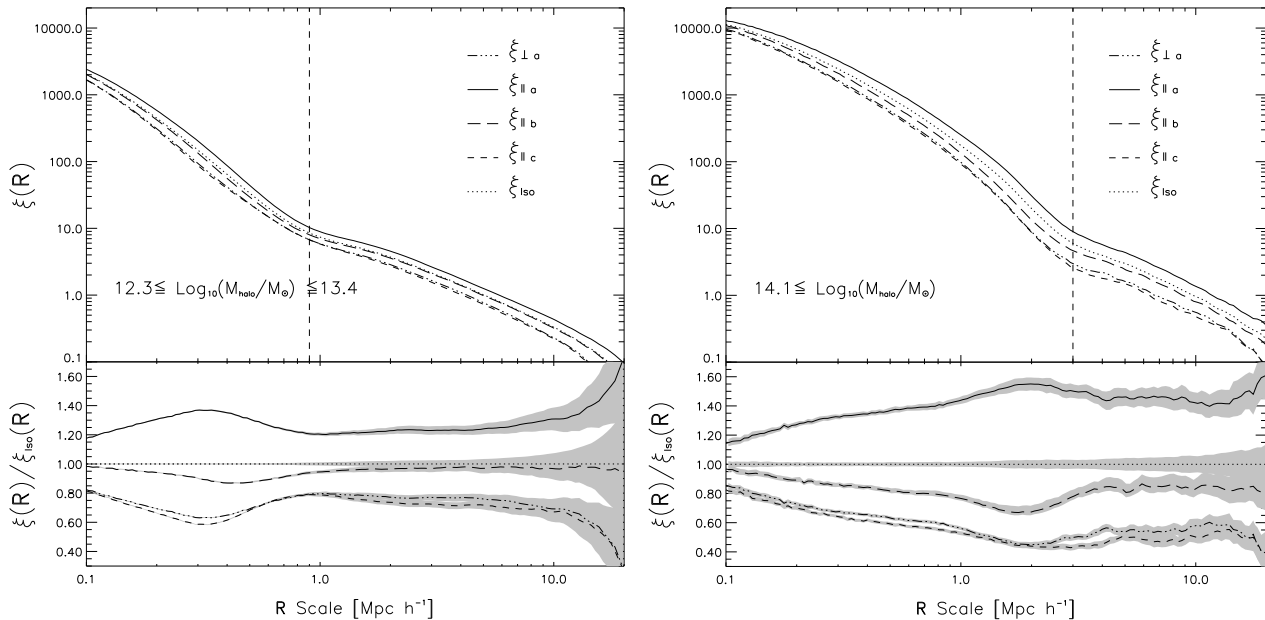


**Figure 1.** Left panel: Spatial Halo–Dark-matter correlation function of low mass halos in the numerical simulation. The solid, long dashed and short dashed lines show the correlation functions between halos and neighbour particles along the directions of the major, intermediate, and minor axes of the halo shape ellipsoid, respectively. The dotted line shows the results for the isotropic correlation function obtained by using all the tracers regardless of the direction (i.e. the classical halo-particle cross-correlation function). The dotted-dashed lines correspond to the correlation function between halos and neighbour particles in the direction perpendicular to the halo shape major axis. The dashed vertical line represents the transition scale between the 1– and 2–halo terms of the cross-correlation function. Shaded areas indicate the  $1\text{-}\sigma$  standard deviation around each measurement. The lower left subpanel shows ratios between the directional and isotropic correlation functions shown in the top-left panel. Right panel: same as left panel, for a high mass DM halo subsample obtained from the simulation.

prolate tendency, while the opposite case,  $b/a > c/b$ , corresponds to a predominantly oblate ellipsoid.

Since we will apply a statistical method to observations, we also construct a synthetic SDSS catalogue in order to test the effects introduced by observational biases. By applying the SDSS selection function on our simulation box we produce a mock catalogue (see for instance, Cole et al. 1998). For simplicity, and because our goal is merely to match the geometry and depth of the catalogue, we compute the radial selection function of simulation particles by randomly assigning them an absolute magnitude. We use different Schechter luminosity functions to apply SDSS r-band magnitudes to the particles. For particles outside groups we use the parameters  $\phi_* = 0.0149$   $M_* = -20.44$   $\alpha = -1.05$  (Blanton et al. 2003), whereas for particles inside groups, we use different Schechter parameters, which depend on the halo mass following (Zandivarez et al. 2006). The flux-limit selection of the mock catalogue is then obtained by imposing the same upper apparent magnitude threshold which affects the observational sample (in our case we consider galaxies with  $m < 17.5$ , in both real and mock catalogues). In order to determine the angular selection function of the survey, we divided the sphere in  $\sim 7,700,000$  pixels using the SDSSPix software. This pixelisation scheme was specifically designed for the SDSS geometry (see for instance Swanson et al. 2008). We then compute an initial binary mask by setting to 1 all pixels with at least one galaxy inside, and 0 the remaining pixels. Given that the pixel size

is quite smaller than the mean inter-galaxy separation, we smooth the initial mask by averaging each pixel over its  $7 \times 7$  adjacent neighbours. We compound the angular selection function as the set of all pixels with a value that exceeds a given threshold. Finally, we construct a SDSS-DR7 mock catalogue from the simulation box, by means of radial and angular selection functions. In addition, a mock group sample is produced from the mock catalogue, by applying the same percolation algorithm used for real groups (see section 3.1). In our mock catalogue, the shapes of groups will be calculated in the same way as in the observational data, i.e. using only the projected positions of group members on the sky.

## 2.2 Three-dimensional Results: anisotropic two point cross-correlation function

We use the spatial halo-particle cross-correlation function  $\xi(r)$  to study the relation between the anisotropy presented by the distribution of matter and the orientation of halo shapes. This cross-correlation function measures the probability excess to find a dark matter particle (tracer) in the volume element  $dV$  at a distance  $r$  from a given halo (centre) (Peebles 1980). A standard method to measure  $\xi(r)$  in a simulation box consists in counting halo-particle pairs in a given distance bin, and normalising this quantity by the expected number of pairs for a homogeneous distribution. Paz et al. (2008) perform these counts restricting the pairs to fixed

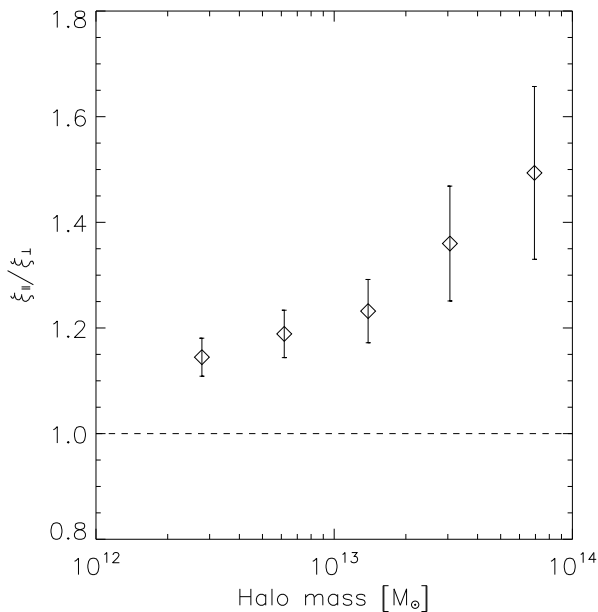


**Figure 2.** Global ratios between three dimensional correlation functions along the directions parallel and perpendicular to the central halo major axis ( $\xi_{\parallel a} / \xi_{\perp a}$ ). This ratio is computed by counting pairs with separations on the 2-halo scale regime. The horizontal dashed line corresponds to a no anisotropy behaviour.

ranges in the angle between their relative position vector and a given direction. In our case, since we estimate the halo-particle cross correlation function, we restrict halo-particle pair counts to different ranges of the angle subtended by its relative position vector and the central halo shape axes (i.e.  $\hat{a}$ ,  $\hat{b}$  or  $\hat{c}$ ). We will refer to the classical cross-correlation function, computed using all pairs regardless of their angle as the “isotropic” cross-correlation function ( $\xi_{\text{iso}}$ ). We define the “parallel” cross-correlation functions as those computed using all pairs subtending an angle with respect to a given halo shape axis smaller than a given threshold  $\theta_1 = 60^\circ$  (we justify this value later in this section). These functions will be denoted  $\xi_{\parallel a}$ ,  $\xi_{\parallel b}$  and  $\xi_{\parallel c}$ , for the corresponding axis  $\hat{a}$ ,  $\hat{b}$  and  $\hat{c}$ .

We will also measure the dependence of the amplitude and shape of the parallel cross-correlation functions on halo mass ( $M_{\text{halo}}$ ). For this purpose, the halos in the simulation are split into five samples with different mass ranges. Figure 1 shows in dotted lines the isotropic halo-particle cross-correlation function  $\xi_{\text{iso}}$  for low mass systems ( $M_{\text{halo}} \leq 2.5 \times 10^{13} M_{\odot} h^{-1}$ , left panel) and high mass systems ( $M_{\text{halo}} \geq 1.3 \times 10^{14} M_{\odot} h^{-1}$ , right panel). The short dashed, long dashed and solid lines correspond to the cross-correlation functions estimated using particles in the direction parallel to the minor, intermediate, and major axes of the halo shape, respectively, as described above. The bottom panels show the ratio between the directional cross-correlation functions and the isotropic function, with the same line styles as in the upper panels. Shaded areas correspond to Jackknife error bands ( $1-\sigma$  uncertainties), estimated using the jackknife technique with a total of 100 subsamples for both, the numerical simulation and the SDSS data. Our

jackknife errors estimations are stable between 20 to 150 subsamples, without error underestimations. We will apply this error estimate throughout this paper.

The halo-particle cross-correlation functions in Figure 1 show the characteristic 1- and 2-halo terms reported in several previous measurements of both, observational (Zehavi & et al. 2004; Yang et al. 2005) and numerical simulations (see for instance Hayashi & White 2008). The dashed vertical line represents the transition scale between 1- and 2-halo terms (where the correlation function has a local minimum in the first derivative).

In Figure 1 it can be seen that the parallel cross-correlation functions along the minor and intermediate halo shape axes ( $\xi_{\parallel c}$  and  $\xi_{\parallel b}$ ), show a lower amplitude than the isotropic classical cross-correlation function ( $\xi_{\text{iso}}$ ), which in turn is smaller than the cross-correlation function measured along the halo major axis direction ( $\xi_{\parallel a}$ ). This measurement can be interpreted as an excess of surrounding large scale structure along the direction of halo major axis. The decrement of correlation power shown by  $\xi_{\parallel c}$  and  $\xi_{\parallel b}$ , could signal a decrement of the particle density in the surrounding matter distribution in the plane perpendicular to the central halo major axis. The drop in the correlation amplitude with respect to the isotropic case observed for the  $\xi_{\parallel b}$  function is smaller than that observed for the  $\xi_{\parallel c}$ . This results reflects the triaxial nature of the structure surrounding a typical halo. In spite of this quantitative difference both,  $\xi_{\parallel b}$  and  $\xi_{\parallel c}$  exhibit a decrement rather than an increment, that could be understood as a weak preference for a triaxial over a prolate configuration for the surrounding structure. For instance, if  $\xi_{\parallel b}$  would showed an increment with respect to the isotropic function in the same way as  $\xi_{\parallel a}$  does, we would have interpreted instead an oblate tendency for the surrounding structure. It is also important to remark that  $\xi_{\parallel b}$  becomes consistent with the isotropic function  $\xi_{\text{iso}}$  at large enough scales.

Given the prolate tendency shown by the cross-correlation function analysis, as well as the similar amplitudes of  $\xi_{\parallel b}$  and  $\xi_{\text{iso}}$ , from this point on, we will only study the anisotropy of the matter distribution around dark matter halos using directions defined by the halo shape major axis. In addition to this, we compute the “perpendicular” cross-correlation function by adding pairs lying an angle  $\theta_2$  or lower from the plane perpendicular to the halo major axis direction. This function is denoted by  $\xi_{\perp a}$ . We choose the threshold angles, for the parallel and perpendicular cases mentioned above ( $\theta_1$  and  $\theta_2$ , respectively), so that the volumes in each case are the same. This can be achieved by setting,  $\sin(\theta_2) = 1 - \cos(\theta_1) = \chi$ , and choosing a value for the threshold parameter  $\chi$ . When different values of  $\chi < 0.5$  are chosen, the angles  $\theta_1$  and  $\theta_2$  tend to acquire more acute values, while maintaining equal volumes. When adopting different values of  $\chi$  we found that the ratios between parallel and perpendicular correlations,  $\xi_{\parallel d} / \xi_{\perp d}$  (where  $d$  represents either axis,  $a$ ,  $b$  or  $c$ ) remain roughly constant, and the significance increases for larger volumes, up to  $\chi = 0.5$ . When the volumes for the parallel and perpendicular correlation are not the same,  $\xi_{\perp d}$  and  $\xi_{\parallel d}$  show different degrees of departure from the isotropic correlation; in particular, the correlation corresponding to the largest volume tends to be more similar to the isotropic case. Consequently, we have selected  $\chi = 0.5$ , which implies angles  $\theta_1 = 60^\circ$  and  $\theta_2 = 30^\circ$ .

This choice ensures that every halo-particle pair contributes to one of the two volumes.

The results for the perpendicular cross-correlation function are shown as dot-dashed lines in Figure 1. As can be seen, its amplitude is quite similar to the parallel cross-correlation function along the minor axis. In fact, over most of the 2-halo regime these two correlation functions are indistinguishable according to the jackknife error bands. Additionally, there is also an important difference between the parallel and perpendicular cross-correlation functions (with respect to the major axis of the halo shape,  $\hat{a}$ ); their relative amplitudes show highly statistically significant differences. The transition between the 1- and 2-halo terms can be clearly seen in the cross-correlation function quotients. Given the halo shape definition (Equation 1) and the aspherical geometry of halos (Paz et al. 2006), it is expected that on scales within the 1-halo term, the parallel and perpendicular cross-correlation functions will present a significant difference, since they will simply mirror the intrinsic halo shapes. A more relevant result is that coming from the comparison between the cross-correlation functions over the 2-halo term regime, which shows an approximately constant behaviour and only loses statistical significance at very large separations. Figure 1 also shows that the anisotropy of the cross-correlation function for the high mass sample (right panel) is higher than for the low mass sample. We have analysed five samples with halo masses ranging from  $10^{12}M_{\odot}h^{-1}$  to  $2 \times 10^{14}M_{\odot}h^{-1}$ , confirming that the 2-halo term alignment signal increases with the halo mass.

As is described above, the anisotropy signal behaviour is approximately constant over the 2-halo clustering regime. Therefore, it is possible to characterise a median alignment signal over this range by counting all pairs with separations in the 2-halo regime, in order to estimate a global quotient between correlation functions along the directions parallel and perpendicular to the halo centre major axis. These results are shown on Figure 2 for five samples constructed using different halo centre mass intervals. The median mass for each sample is shown on the abscissas, whereas the ordinate shows the global ratio  $\xi_{\parallel a}/\xi_{\perp a}$ . Error bars are estimated using the jackknife resampling technique. As can be seen in the figure, there is an increment of the degree of anisotropy as the mass increases. This is expected in the hierarchical halo formation scenario since more massive halos have more recent formation epochs and therefore they are more likely to be aligned with the present large scale matter distribution.

### 2.3 Projected anisotropic cross-correlation function and resolution effects

The analysis of observational data from redshift surveys is mainly limited by three important effects. (i) The measurement of galaxy group shapes needs to be done in projection on the plane of the sky due to the presence of galaxy peculiar velocities which affect distance estimations based on redshift measurements. In order to assess the reliability of the estimates of projected group shape orientations, it is necessary to reproduce this effect in the simulation, and to study whether the alignment signals can still be detected in this case. The group shape tensor will therefore be calculated using only two directions along the plane of the sky. Due to the flux-limited nature of galaxy catalogues, (ii) only a few

group members are available to estimate the shape tensor, and (iii) the number of tracers is diluted as the distance increases (both effects become stronger at higher redshifts). The decrement of galaxy group members (ii) tends to produce deviations of the estimated group shape orientation with respect to the real direction. This is a shot noise type effect which also biases the measured shapes towards oblate spheroids (Paz et al. 2006). The dilution of the number density of galaxies with redshift can be taken into account with a proper modelling of the selection function of the catalogue via, for instance, constructing mock catalogues. We must estimate the influence of all these effects before proceeding further with the analysis of the real data.

We start by projecting the simulated volume onto the Cartesian plane  $x-y$  in the numerical simulation. This plane resembles the “plane of the sky” of the observational data. The third Cartesian coordinate  $z$  plus the  $z$ -component of the peculiar velocity, is used to estimate a radial velocity along the “line of sight”. This last quantity mimics the redshift measured in observations. The effects of low number statistics on the measured group shapes can be taken into account by selecting at random a small number of particle members in order to compute the projected shapes. Even though galaxies in groups do not necessarily follow the dark matter halo density profile, Paz et al. (2006) have shown that this procedure reproduces the biases present in the observational estimates of group shapes due to projection and shot noise effects, that is, the shapes of simulated dark matter halos measured this way exhibit indistinguishable differences with shapes obtained from galaxy groups in both, real and mock catalogues.

We now perform the equivalent of the analysis presented in section 2.2, using anisotropic projected two-point cross-correlation functions. In an analogous manner to the method implemented on the three-dimensional case, we separate halo-particle pairs according to the angle subtended with respect to the apparent halo major axis. Pairs with angles greater than and less than a threshold angle of  $\theta_p = 45^\circ$ , define the parallel ( $\omega_{\parallel}$ ) and perpendicular ( $\omega_{\perp}$ ) projected cross-correlation functions respectively. Notice that this choice of  $\theta_p$  is analogous to that of  $\theta_1$  and  $\theta_2$  for the three dimensional case, since this separates the plane of the sky in two equal areas. The quotients  $\omega_{\parallel}/\omega_{\perp}$ , for smaller fractions of the area of the sky are roughly constant with a decreasing statistical significance (due to a lower number of counts). This behaviour is analogous to the observed in the three dimensional signal. As a means to avoid a large amount of foreground and background structures we only consider neighbours in distance slices of  $50 \text{ Mpc h}^{-1}$  around the halo centres. Differences between the correlation amplitudes of  $\omega_{\parallel}$  and  $\omega_{\perp}$  will then be interpreted as statistical excesses of the surrounding large scale structure along the direction of the central group projected major axis. This will represent a lower limit of the real anisotropy around the group major axis given the averaging of the orientation of the 3D shape major axis with respect to the line of sight.

With the purpose of studying the dependence of the anisotropy with the mass, we will measure the cross-correlation functions selecting halo centres separated into three mass ranges corresponding to the terciles of the Sloan group mass distribution (see section 3.1 for the description of the group sample). This choice allows a closer comparison

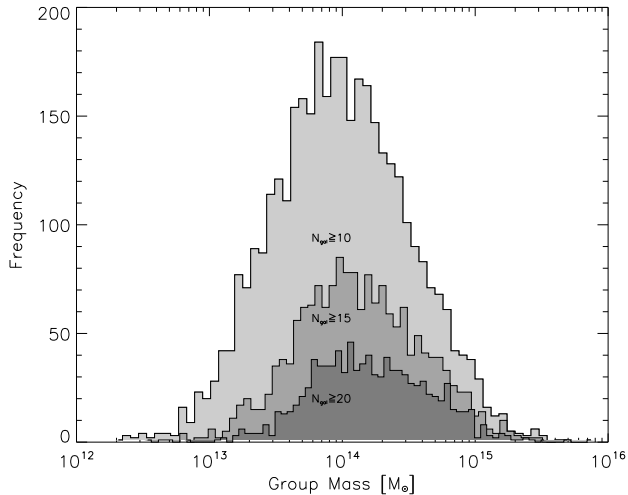


**Figure 3.** Distribution of group masses for different samples selected according to minimum thresholds on number of galaxy members. The lighter shaded histogram shows the results for the main galaxy group sample. Distributions of galaxy group subsamples with more than 15 and 20 galaxy members are shown with darker shaded areas as indicated in the figure key.

with the observational data, and ensures the same number of galaxy groups in each mass range in the observational analysis (see section 3.2). On the other hand, it is well known that the estimate of a halo shape depends on the number of members used to compute it (Paz et al. 2006). Therefore, it is expected that this will affect the alignment signal obtained from the ratios between anisotropic and isotropic cross-correlation functions. In order to analyse the extent of this effect we compute the halo shapes using only 10, 15 and 20 random particles from each halo. Furthermore, to better mimic observations we impose that the distributions of halo mass resemble the real galaxy group distributions with 10, 15 and 20 members, respectively (see Figure 3).

Figure 4 shows the anisotropic projected halo-particle cross-correlation functions for the third tercile on the mass of groups with at least 10 members ( $M_{\text{halo}} \geq 1.7 \times 10^{14} M_{\odot} h^{-1}$ ). The halo major axis direction was determined using 10 particles selected at random. Solid, dotted and dashed lines correspond to parallel, isotropic and perpendicular cross-correlation functions to major axis, respectively. The lower panels show the quotients between anisotropic and isotropic cross-correlation functions. By comparing this figure with right panel of Figure 1 it can be seen that the alignment signal decreases by approximately a 75% due to shot noise and projection effects. It can also be seen that the quality of the signal decreases, lowering the statistical significance by some degree. However, the detection of the alignments remains strong. The error bars decrease significantly when 20 particle members are used in the estimate of the major axis direction.

So far, we have studied the combined effect of projection and shot noise; a third effect mentioned at the beginning of this section, the flux-limited nature of observational catalogues, needs to be analysed. To this end, we use artificial data sets that resembles the real SDSS-DR7 catalogue (see Section 2.1) and the real galaxy group catalogue.

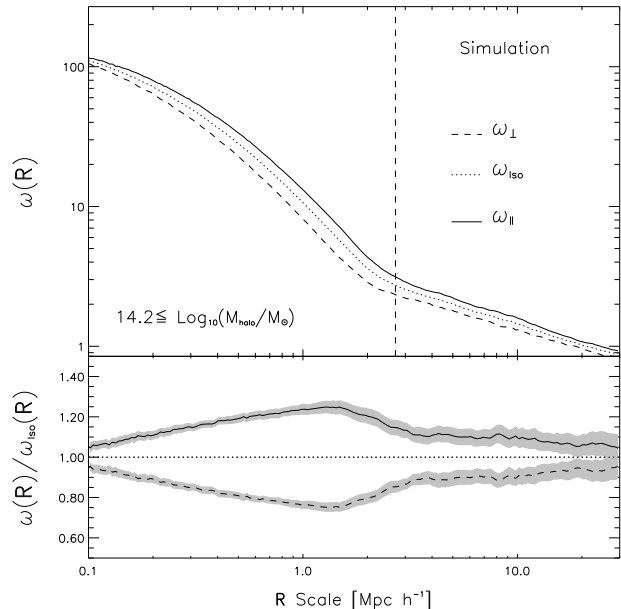


**Figure 4.** Anisotropic projected correlation functions for massive halos (third tercile) with a major axis direction determined using only 10 randomly selected particles. The mass distribution was forced to resemble the corresponding real galaxy group mass distributions with 10 members.

Based on this mock data we compute again the parallel ( $\omega_{\parallel}$ ) and perpendicular ( $\omega_{\perp}$ ) projected group-galaxy cross-correlation functions, by applying the same procedure used on the observations, as will be described in the following sections (see Section 3.2). The results are shown in Figure 5. Line types are as in Figure 4. The first three panels (A, B and C) show the projected anisotropic cross-correlation functions for different mass terciles, for mock groups with at least 10 galaxy members. In the lower right panel of Figure 5 (panel D) we show the results for mock groups in the highest mass tercile with at least 20 group members.

We now compare the results from projected and three dimensional correlation functions with the aim to assess the degree of loss of the alignment signal of section 2.2. The analysis of the expected biases allows us to conclude that the alignment signal obtained in section 2.2 is still detectable on projected measurements of the two point cross-correlation function. When only considering the effect of projection we find, for scales around  $10 \text{ Mpc } h^{-1}$ , differences between correlation quotients in the directions parallel and perpendicular to the halo orientation decrease by a 50%, with respect to the corresponding three-dimensional ratio (Figure 1 right panel). When the mass distribution of observational galaxy groups is reproduced (Figure 3), and also the discreteness effect on the determination of group shapes is taken into account (Figure 4), the anisotropy signal diminishes even more, another 50% at scales around  $10 \text{ Mpc } h^{-1}$ , that is a 75% with respect to the quotients shown in Figure 1. Finally, when the depth and geometry of the observational survey are taken into account, as well as the galaxy group identification is mimic, the error bars increase significantly. However, the anisotropy signal remains detectable with a high statistical significance over a wide range of distances.

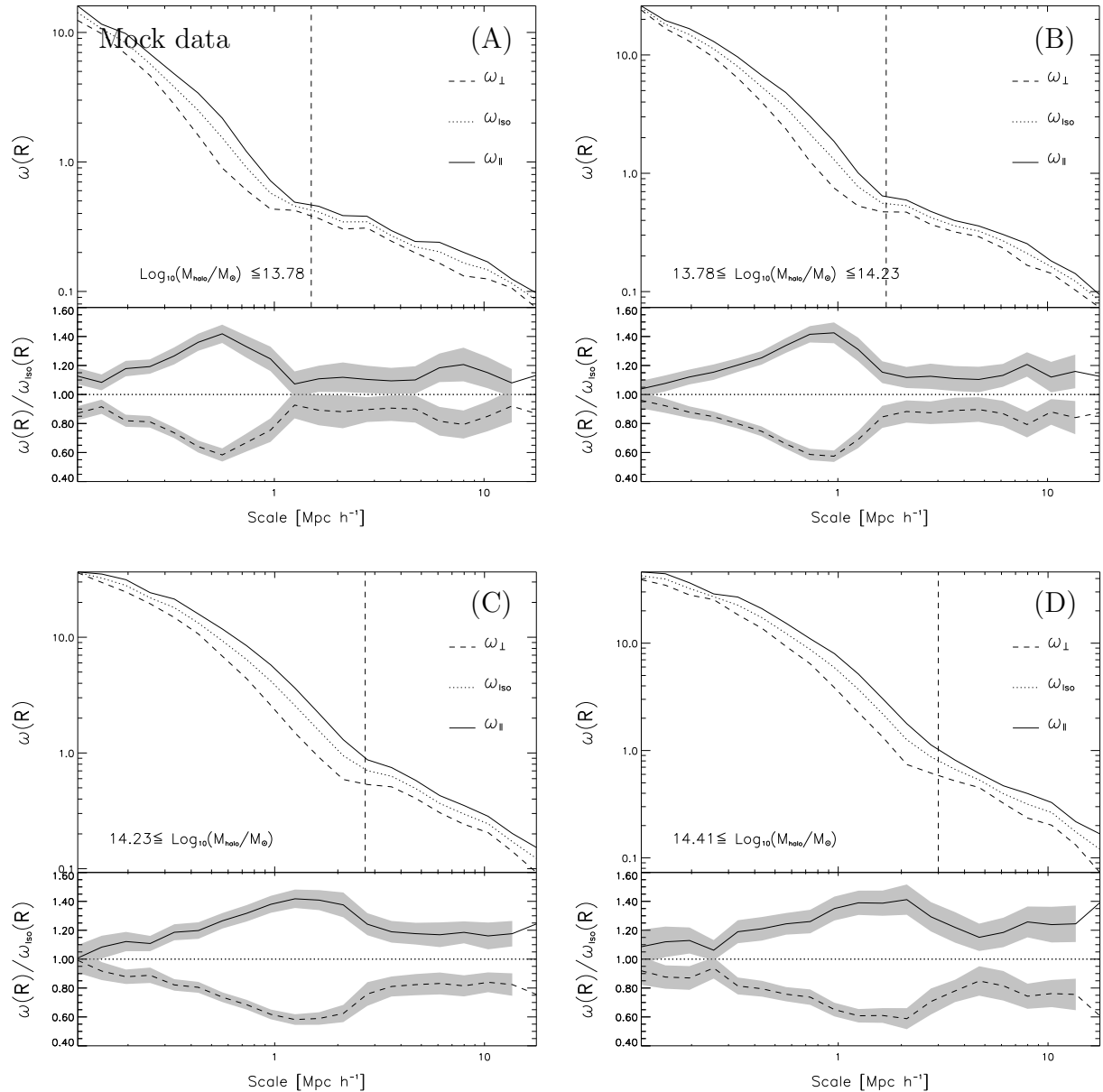


**Figure 5.** Projected group–galaxy correlation functions for three group mass ranges extracted from a mock SDSS catalogue. The dashed lines correspond to the correlation function between mock groups and mock neighbour galaxies in the direction perpendicular to the group shape major axis, as seen projected onto the sky. The solid lines show the results when using tracers along the direction of the projected major axis, and the dotted lines show the corresponding results when all neighbours are taken into account. The first three panels, A, B and C, show the results for the lowest, intermediate and highest mass terciles of the mock galaxy group sample selected with at least 10 mock galaxy members per group. The lower right panel, labelled D, shows the results for the high mass tercile with at least 20 members ( $M \geq 2.6 \times 10^{14} h^{-1} M_{\odot}$ ). The ratios between the correlation functions along different directions and the correlation function obtained using all the neighbours are shown in the lower subpanels.

### 3 OBSERVED CORRELATION ALIGNMENTS ON SDSS REAL DATA

In this section we analyse the presence of galaxy group shape alignments with the large scale structure as traced by real galaxies. To this end, measurements of anisotropic projected cross-correlation functions were performed searching for an alignment signal in the 1–halo and 2–halo clustering regimes. At the end of this Section we provide a comparison between observational and numerical simulation results.

#### 3.1 The galaxy group sample

We use the main galaxy sample from the 7th Data Release of the Sloan Digital Sky Survey (SDSS-DR7, Abazajian & et al. 2009) which includes roughly  $\approx 900,000$  galaxies with redshift measurements to  $z \approx 0.3$  and an upper apparent magnitude limit of 17.77 in the r band. The galaxy groups used in this work have been identified in this sample using the same procedure as in Merchán & Zandivarez (2005). The method consists in using a friend-of-friend al-

gorithm similar to the one developed by Huchra & Geller (1982). The algorithm links pairs of galaxies ( $i, j$ ) which satisfy  $D_{ij} \leq D_0 R(z)$  and  $V_{ij} \leq V_0 R(z)$  where  $D_{ij}$  is the projected distance and  $V_{ij}$ , the line-of-sight velocity difference. The scaling factor  $R(z) \propto n_g^{-3}$  is introduced in order to take into account the decrement of the observed galaxy number density,  $n_g$ , with redshift due to the apparent magnitude limit cutoff (see eq. 5 in Huchra & Geller 1982). We have adopted a transverse linking length  $D_0$  corresponding to an overdensity of  $\delta\rho/\rho = 80$ , a line-of-sight linking length of  $V_0 = 200 \text{ km s}^{-1}$  and a fiducial distance of  $10 \text{ Mpc h}^{-1}$ . Our main group sample comprises all galaxy groups with at least 10 galaxy members. Group virial masses are estimated following Merchán & Zandivarez (2005); Limber & Mathews (1960),

$$M = \frac{\sigma^2 R_v}{G},$$

where  $\sigma$  is the three dimensional velocity dispersion,  $R_v$  is the virial radius (see eq. 6 in Merchán & Zandivarez 2005) and  $G$  is the gravitational constant. The velocity dispersion  $\sigma$  is estimated using its observational counterpart, the line-of-sight velocity dispersion  $\sigma_v$ ,  $\sigma = \sqrt{3}\sigma_v$ .

Figure 3 shows the mass distribution for the main group sample and for two additional subsamples with at least 15 and 20 galaxy members. In order to analyse the dependence of any alignments with mass, we divide the ordered mass distribution in three parts, each containing a third of the sample population. The halo mass distribution shifts and stretches to higher masses when a higher minimum number of galaxy members is imposed.

### 3.2 Observed alignments on the projected cross-correlation function

In section 2.2 the correlation function measured in the simulation was estimated by counting halo-particle pairs and normalising by the expected number of pairs for a homogeneous distribution. Due to the complex selection function of the SDSS survey, it is necessary to produce a random distribution of points with the same selection function in order to normalise the group-galaxy pair counts. This normalisation can be done in several ways; in this work we use two estimators, the classic estimator (Davis & Peebles 1983)  $\omega = DD/DR - 1$ , where  $DD$  and  $DR$  are the numbers of *group-galaxy* and *group-random* pair counts respectively, and a symmetric version of the Landy & Szalay (1993) estimator; in all cases we find negligible differences between these two estimators. We perform all the analysis using the Landy & Szalay estimator. This computation is performed as  $\omega = (DD - DR - RD + RR)/RR$ , where in addition to  $DD$  and  $DR$ , we need to calculate  $RR$  and  $RD$ , the numbers of *random centre-random tracer* and *random centre-galaxy* pair counts respectively. For each sample of groups we compute a random centre catalogue that mimic its redshift distribution. The number of random centres is about 100 times the number of groups in each sample. The homogeneous sample of tracers was computed from the expected numerical density of galaxies at a given redshift, with a magnitude below the limit of the survey, and a Schechter luminosity distribution with parameters  $\phi_* = 0.0149$ ,  $M_* = -20.44$ ,  $\alpha =$

$-1.05$  (Blanton et al. 2003). These random catalogues contain  $2 \times 10^7$  random points. The angular positions are restricted to the angular mask described in section 2.3.

In order to estimate the galaxy group anisotropic cross-correlation function we follow the same definitions given in section 2.3 (i.e.  $\omega_{\parallel}$ ,  $\omega_{\perp}$ ,  $\omega_{\text{iso}}$ ). We therefore count  $DD$  and  $DR$  pairs depending on their relative orientation with the major projected axis of the group shape tensor. These counts are binned over a wide range of scales covering from 0.1 to  $50 \text{ Mpc h}^{-1}$ . In analogy with the estimate of the projected cross-correlation function in simulations (section 2.3), we only consider galaxy neighbours with relative comoving distance  $< 50 \text{ Mpc h}^{-1}$  around the group centre.

In Figure 6 we show the resulting cross-correlation function measurements. Line types are as in Figure 4. The first three panels (A, B and C) show the projected anisotropic cross-correlation functions for different mass terciles, for groups with at least 10 galaxy members. In order to study the effect of low number statistics, we repeat the same analysis for samples with more than 15 and 20 galaxy members. For simplicity only the results from the highest mass tercile are shown in panel D of Figure 6, for groups with at least 20 galaxy members.

The first three panels in Figure 6, show a similar behaviour to that seen in the numerical simulation, where the anisotropy signal increases with mass, particularly for the 2-halo regime. In other words, significant statistical differences are seen between the  $\omega_{\parallel}$  and  $\omega_{\perp}$  projected cross-correlation functions, which become more prominent as the mass of the centre group increases. The number of galaxy groups used to compute the results showed in panel D is approximately a third of the total number of groups. Consequently, the correlation function errors increase. Nevertheless, the signal is still significant. A striking similarity of the results on this figure with the corresponding mock results can be observed by direct comparison with Figure 5.

The results shown in this section confirm the presence of alignments in the large-scale structure as traced by galaxies and the direction of the major axis of galaxy groups, in qualitative agreement with the expectations from  $\Lambda$ CDM model. This alignment signal persist over the two halo regime, up to scales of  $20 \text{ Mpc h}^{-1}$ , pointing an alignment between the group inner galaxy distribution and the surrounding large scale structure.

It should also be mentioned that the covariance matrix of the correlation function has non-zero off-diagonal elements. In order to reduce the effects of covariance between measurements at different scales, we estimated global ratios between cross-correlation functions in the directions perpendicular and parallel to the group major axes on two different wide scale ranges, corresponding to the 1- and 2-halo terms, characterised by projected distances lower and greater than a transition scale. This procedure allows to diminish the effect of error correlations on the anisotropy, and also allows to study the alignments on these two different scale regimes. The scale threshold depends on mass, varying from 0.5 to  $3 \text{ Mpc h}^{-1}$  over the mass range considered here.

Figure 7 shows the 1- and 2-halo term ratios as a function of the average subsample mass (left and right panels, respectively). In the figure the open symbols represent the results obtained from real observational data, whereas



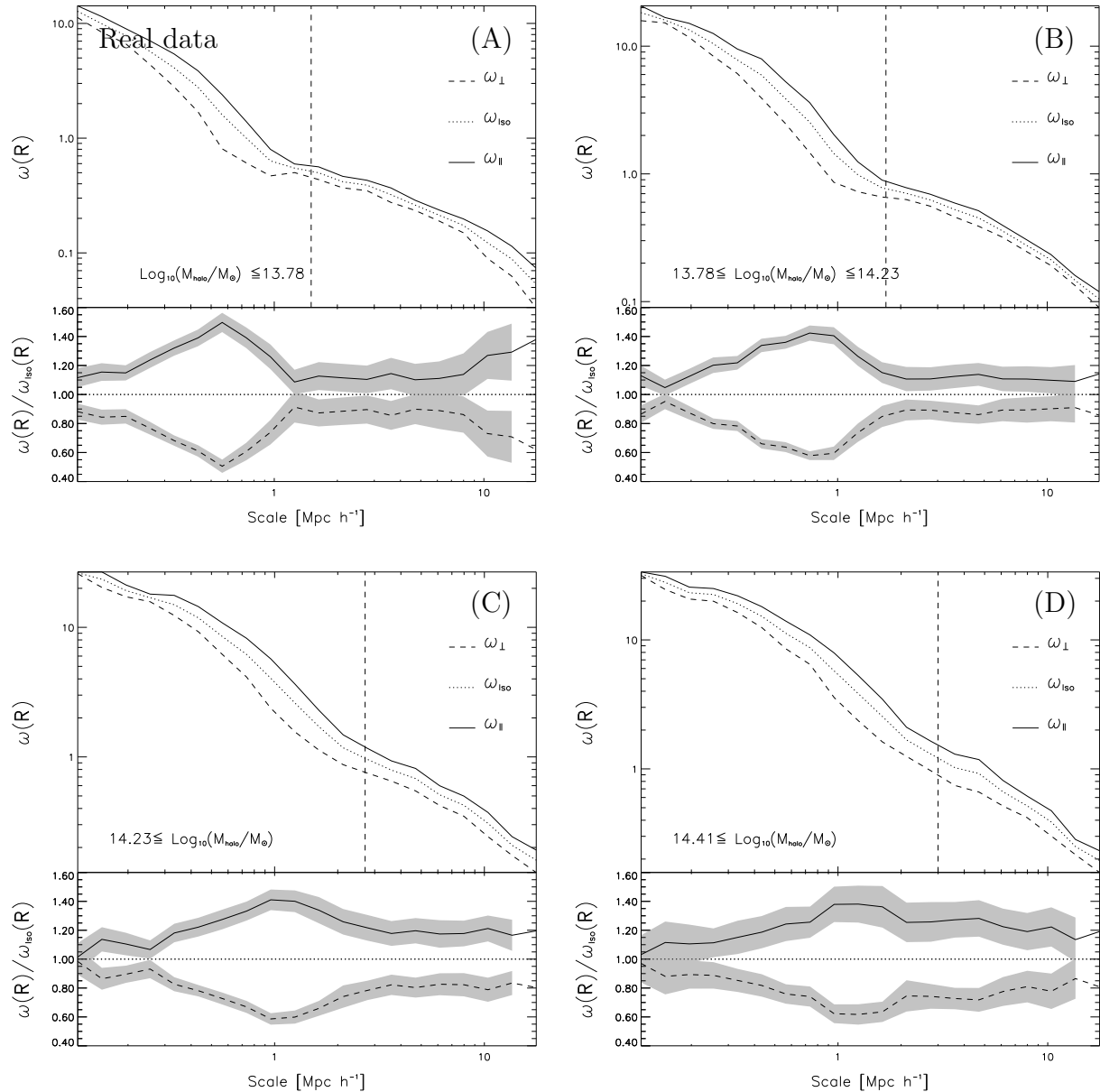


**Figure 6.** SDSS projected group–galaxy correlation functions for three group mass ranges. The dashed lines correspond to the correlation function between groups and neighbour galaxies in the direction perpendicular to the group shape major axis, as seen projected onto the sky. The solid lines show the results when using tracers along the direction of the projected major axis, and the dotted lines show the corresponding results when all neighbours are taken into account. The first three panels, A, B and C, show the results for the lowest, intermediate and highest mass terciles of the galaxy group sample selected with at least 10 galaxy members per group. The lower right panel, labelled D, shows the results for the high mass tercile with at least 20 galaxy members ( $M \geq 2.6 \times 10^{14} h^{-1} M_{\odot}$ ). The ratios between the correlation functions along different directions and the correlation function obtained using all the neighbours are shown in the lower subpanels.

filled symbols correspond to mock data described in section 2.3. As shown in the figure key, the different open (filled) symbols represent measurements obtained from real (mock) group samples with at least 10, 15 and 20 galaxy group members. This figure can be used to analyse the dependence of the anisotropy on the group mass for the 1– and 2–halo regimes in real and simulated data.

The 1–halo term ratios obtained from the numerical simulation reflect a slight increase in the asphericity of halos as their mass increases, which is qualitatively consistent with

previous results on the projected shapes of galaxy groups Paz et al. (2006). The observations do not show a clear tendency, although error bars do not allow a clear distinction between mock and real data, indicating that the use of the shape tensor is more adequate for the purposes of studying the variation of the intrinsic shape of groups as a function of mass. In most cases the observations are in agreement with the numerical simulation results.

On the 2–halo regime, the ratios shows a marginal increase with the group mass, both in the numerical simula-

tion and observational results, which do not show a systematic dependence on the minimum number of group members used. Within the uncertainties, the observational results are in agreement with mock data. It can be seen for all mass samples, regardless of the number of group members, a significant degree of anisotropy in the correlation ratios. For the more massive sample this anisotropy is distinguishable from isotropy at a level above 3 standard errors.

#### 4 CONCLUSIONS

We have used a technique developed by Paz et al. (2008) to characterise the alignment between the shape of gravitationally bound systems and the large scale structure on a  $\Lambda$ CDM numerical simulation and observed galaxy groups taken from the Sloan Digital Sky Survey, Data Release 7. We have detected a statistically significant alignment of galaxy groups with the surrounding large scale structure traced by SDSS spectroscopic galaxies. This result, based on an up-to-date sample of spectroscopic galaxy groups, supports the well known theoretical alignment of dark matter halo shapes with the circumventing large scale structure.

The analysis on the  $\Lambda$ CDM numerical simulation shows that the direction of maximum elongation of dark matter halos is aligned with the surrounding matter distribution on scales of up to  $30 \text{ Mpc h}^{-1}$ . The resulting halo-particle cross-correlation function shows the characteristic transition between the 1– and 2–halo terms regimes which is also reflected in the anisotropy signal. Given that the 1–halo term corresponds to the inner matter distribution of the halos, the alignment on this range of scales was expected. More interesting to consider is the signal observed over the 2–halo term regime, which could be related with the halo formation history. It has been established that halo formation occurs by anisotropic mergers with lower mass halos. These accretion events occur along directions traced to some extent by the large scale structure. Therefore, the existence of a remnant correlation between halo shape orientations and the large scale matter distribution is expected. This constitutes a fossil record of the halo formation process. Due to the hierarchical nature of halo formation, an increasing anisotropy signal as the halo mass increases is also expected, as more massive halos finished assembling their mass more recently and therefore they are more likely to bear marks of more recent important formation processes. This mechanism also explains the shape-mass relation observed in the SDSS galaxy group sample Paz et al. (2006).

Our measurements of this alignment on the two different halo model regimes are qualitatively consistent with previous results on dark matter halo alignments in  $\Lambda$ CDM numerical studies (Aragón-Calvo et al. 2007; Hahn et al. 2007; Brunino et al. 2007; Cuesta et al. 2008; Patiri et al. 2006; Basilakos et al. 2006). The most extended methodology along the literature, consists on performing statistics over different ranges in the relative angle defined by the halo major axis and the direction to larger structures defined via particular geometrical criteria. For instance, Basilakos et al. (2006), found that cluster sized halos are aligned with their parent supercluster, in agreement with our results. The main asset of our approach is that it allows a robust comparison between numerical simulations and observational data, in-

dependently of any particular characterisation of the surrounding structure. Given that the correlation function can be easily extended from three dimensions to projected data, this comparison arises naturally.

Regarding the results in three dimensions, we have demonstrated that cross-correlation functions with tracers in the directions parallel to the minor and intermediate halo shape axes ( $\xi_{\parallel c}$  and  $\xi_{\parallel b}$ ), show lower correlation amplitudes than the cross-correlation function measured along the major axis ( $\xi_{\parallel a}$ ) up to scales of  $30 \text{ Mpc h}^{-1}$ . We also found important differences between the parallel and perpendicular cross-correlation functions (with respect to the major halo axis  $\hat{a}$ ). The detected correlation anisotropy signal was interpreted as a decrement of the typical particle density in the surrounding matter distribution in the plane perpendicular to the central halo major axis. We also showed that the alignment signal is higher as the central halo sample mass increases.

In order to confront simulations and observations, we have analysed the effect of projections, group mass distribution and shot noise using the numerical simulation. The alignment signal remains detectable, with an important statistical significance level over a wide range of distances.

The key result of the present study is the observational detection and quantification of a large scale anisotropy around galaxy groups. In agreement with full numerical simulations and mock catalogue results, our measurements of the projected two point cross-correlation function for SDSS groups and galaxies, exhibit an important degree of anisotropy. This signal is observed as a difference in the correlation amplitude estimated in the directions parallel and perpendicular to the group projected major axis. As expected, the amplitude of this feature increases with the average mass of the groups. The observed anisotropy is detected for group masses greater than  $\simeq 6 \times 10^{13} M_{\odot}$ , and its statistical significance increases with the group mass.

We average the alignment effect over ranges of scales corresponding to the 1– and 2–halo terms in the cross-correlation function. The 1–halo term results show similar anisotropies in the numerical simulation and the SDSS, and are consistent with the known increase of asphericity as the group mass increases (Paz et al. 2006), a trend that is clearly detected in the numerical simulation and only mildly present in the observational sample of groups; this simply indicates that direct measurements of group shape (e.g.  $b/a$ ) are more suited to detect this trend.

The 2–halo regime shows an excellent agreement between the mock model and observations. We find that the alignment of the shape of groups with the large-scale structure increases with the halo mass reflecting the fact that higher mass groups have had, on average, more recent merger activity and therefore, younger dynamical ages. This result is independent of the number of group members used, indicating its lack of sensitivity to the shot-noise effect that biases group shape estimates (i.e. it affects the shape more strongly than the direction of the group major axis). The excellent quantitative agreement between observations and the  $\Lambda$ CDM model results provides new direct evidence of the adequacy of the gravitational instability to describe the large-scale structure formation of our Universe.

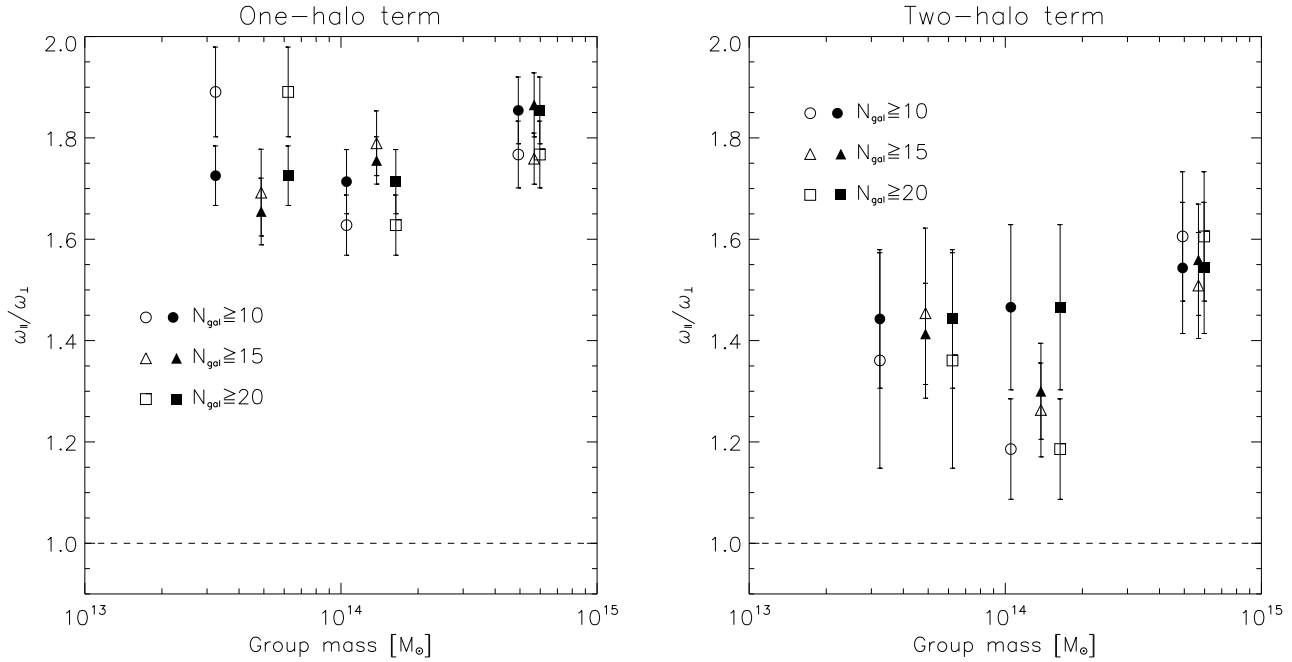


**Figure 7.** Global ratios between correlation functions along the directions parallel and perpendicular to the central group projected major axis ( $\omega_{\parallel}/\omega_{\perp}$ ). Two different ratios are computed by counting pairs split into the 1- and 2-halo clustering regimes (left and right panels respectively). The open symbols represent the results obtained from real observational data. Filled symbols show the corresponding results obtained from the SDSS mock catalogue. The horizontal dashed lines indicate the unit ratio (no anisotropy).

## ACKNOWLEDGEMENTS

DP, MS and MM acknowledge support from CONICET and SECyT, Universidad Nacional de Córdoba. DP acknowledges receipt of a postdoctoral fellowship from CONICET. NP acknowledges support from Fondecyt Reg. 1071006, FONDAP CFA 15010003, and BASAL CATA PFB-06.

## REFERENCES

- Abazajian K. N., et al. 2009, *ApJS*, 182, 543  
Allgood B., Flores R. A., Primack J. R., Kravtsov A. V., Wechsler R. H., Faltenbacher A., Bullock J. S., 2006, *MNRAS*, 367, 1781  
Altay G., Colberg J. M., Croft R. A. C., 2006, *MNRAS*, 370, 1422  
Aragón-Calvo M. A., van de Weygaert R., Jones B. J. T., van der Hulst J. M., 2007, *ApJL*, 655, L5  
Basilakos S., Plionis M., Yepes G., Gottlöber S., Turchaninov V., 2006, *MNRAS*, 365, 539  
Bett P., Eke V., Frenk C. S., Jenkins A., Helly J., Navarro J., 2007, *MNRAS*, 376, 215  
Binggeli B., 1982, *A&A*, 107, 338  
Blanton M. R., Hogg D. W., Bahcall N. A., Brinkmann J., Britton M., Connolly A. J., 2003, *ApJ*, 592, 819  
Brunino R., Trujillo I., Pearce F. R., Thomas P. A., 2007, *MNRAS*, 375, 184  
Colberg J. M., Krughoff K. S., Connolly A. J., 2005, *MNRAS*, 359, 272  
Cole S., Hatton S., Weinberg D. H., Frenk C. S., 1998, *MNRAS*, 300, 945  
Cuesta A. J., Betancort-Rijo J. E., Gottlöber S., Patiri S. G., Yepes G., Prada F., 2008, *MNRAS*, 385, 867  
Davis M., Peebles P. J. E., 1983, *ApJ*, 267, 465  
De Lucia G., Springel V., White S. D. M., Croton D., Kauffmann G., 2006, *MNRAS*, 366, 499  
de Theije P. A. M., Katgert P., van Kampen E., 1995, *MNRAS*, 273, 30  
Faltenbacher A., Li C., White S. D. M., Jing Y., Shu-DeMao Wang J., 2009, *Research in Astronomy and Astrophysics*, 9, 41  
Godłowski W., Flin P., 2010, *ApJ*, 708, 920  
Hahn O., Porciani C., Carollo C. M., Dekel A., 2007, *MNRAS*, 375, 489  
Hayashi E., White S. D. M., 2008, *MNRAS*, 388, 2  
Hopkins P. F., Bahcall N. A., Bode P., 2005, *ApJ*, 618, 1  
Huchra J. P., Geller M. J., 1982, *ApJ*, 257, 423  
Kasun S. F., Evrard A. E., 2005, *ApJ*, 629, 781  
Lagos C. D. P., Padilla N. D., Cora S. A., 2009, *MNRAS*, 397, L31  
Landy S. D., Szalay A. S., 1993, *ApJ*, 412, 64  
Lau E. T., Nagai D., Kravtsov A. V., Zentner A. R., 2010, *ArXiv e-prints*  
Limber D. N., Mathews W. G., 1960, *ApJ*, 132, 286  
Merchán M. E., Zandivarez A., 2005, *ApJ*, 630, 759  
Onuora L. I., Thomas P. A., 2000, *MNRAS*, 319, 614  
Patiri S. G., Cuesta A. J., Prada F., Betancort-Rijo J., Klypin A., 2006, *ApJ*, 652, L75  
Paz D. J., Lambas D. G., Padilla N., Merchán M., 2006, *MNRAS*, 366, 1503  
Paz D. J., Stasyszyn F., Padilla N. D., 2008, *MNRAS*, 389, 1127  
Peebles P. J. E., 1980, *The large-scale structure of the universe*  
Plionis M., 1994, *ApJS*, 95, 401  
Power C., Navarro J. F., Jenkins A., Frenk C. S., White

- S. D. M., Springel V., Stadel J., Quinn T., 2003, MNRAS, 338, 14
- Ragone-Figueroa C., Plionis M., Merchan M., Gottlober S., Yepes G., 2010, ArXiv e-prints
- Rhee G., van Haarlem M., Katgert P., 1992, AJ, 103, 1721
- Rhee G. F. R. N., Katgert P., 1987, A&A, 183, 217
- Richstone D., Loeb A., Turner E. L., 1992, ApJ, 393, 477
- Robotham A., Phillipps S., De Propris R., 2008, ApJ, 672, 834
- Splinter R. J., Melott A. L., Linn A. M., Buck C., Tinker J., 1997, ApJ, 479, 632
- Springel V., 2005, MNRAS, 364, 1105
- Struble M. F., Peebles P. J. E., 1985, AJ, 90, 582
- Swanson M. E. C., Tegmark M., Hamilton A. J. S., Hill J. C., 2008, MNRAS, 387, 1391
- Thomas P. A., Colberg J. M., Couchman H. M. P., Efstathiou G. P., Frenk C. S., Jenkins A. R., Nelson A. H., Hutchings R. M., Peacock J. A., Pearce F. R., White S. D. M., 1998, MNRAS, 296, 1061
- van Haarlem M., van de Weygaert R., 1993, ApJ, 418, 544
- Wang Y., Park C., Yang X., Choi Y., Chen X., 2009, ApJ, 703, 951
- Warren M. S., Quinn P. J., Salmon J. K., Zurek W. H., 1992, ApJ, 399, 405
- West M. J., 1989a, ApJ, 344, 535
- West M. J., 1989b, ApJ, 347, 610
- West M. J., Jones C., Forman W., 1995, ApJL, 451, L5+
- Yang X., Mo H. J., van den Bosch F. C., Weinmann S. M., Li C., Jing Y. P., 2005, MNRAS, 362, 711
- York D. G., et al. 2000, AJ, 120, 1579
- Zandivarez A., Martínez H. J., Merchán M. E., 2006, ApJ, 650, 137
- Zehavi I., et al. 2004, ApJ, 608, 16
- Zhang Y., Yang X., Faltenbacher A., Springel V., Lin W., Wang H., 2009, ApJ, 706, 747